Maximization of carbon nanotube yield by solid carbon-assisted dewetting of iron catalyst films

Rahul Rao [a, b, *], Jennifer Carpena-Núñez [a, b], Nicholas T. Dee [d], Dmitri N. Zakharov [c], J. Anibal Boscoboinik [c], Eric A. Stach [e], A. John Hart [d], Benji Maruyama [a]

[a] Materials and Manufacturing Directorate, Air Force Research Laboratory, Wright-Patterson Air Force Base, Dayton, OH, 45433, USA
[b] UES Inc., Dayton, OH, 45432, USA
[c] Center for Functional Nanomaterials, Brookhaven National Laboratory, Upton, NY, 11973, USA
[d] Department of Mechanical Engineering, Massachusetts Institute of Technology, Cambridge, MA, 02139, USA
[e] Department of Materials Science and Engineering, University of Pennsylvania, Philadelphia, PA, 19014, USA

A B S T R A C T

Further understanding of how nanoparticle catalyst composition influences the yield of carbon nanotubes (CNTs) is key to their scalable, cost-effective manufacture. In particular, the role of trace carbon deposits on promoting CNT nucleation from the catalyst has been studied recently by our team. Here, we show that deposition of solid carbon onto an iron catalyst film prior to dewetting effectively amplifies the CNT yield. We investigated the effect of the amount of C and Fe on particle formation and reduction, and growth kinetics using a combination of *in situ* techniques – Raman spectroscopy, X-ray photoelectron spectroscopy and environmental transmission electron microscopy. We found that CNT growth rate and yield are maximized for specific relative thicknesses of C and Fe (~0.2 and 0.8 nm, respectively). The presence of carbon causes accelerated dewetting of the catalyst, and more rapidly forms a population of metallic Fe particles that grow CNTs at a higher yield. These factors also cumulatively result in a lower incubation time and improved yield. Therefore, loading of catalyst particles with solid carbon is a straightforward and practical route towards boosting CNT yield and improving the efficiency of CNT growth by chemical vapor deposition.

© 2020 Elsevier Ltd. All rights reserved.

1. Introduction

In catalytic processes, the evolution of a thin film catalyst—from formation of particles to dynamic restructuring at reaction conditions—can dramatically affect the efficiency of the catalyst as well as the resulting product [1,2]. This is especially relevant for CNT growth by catalytic chemical vapor deposition (CVD), where as a result of low nucleation probability and catalyst deactivation, the overall efficiency of most CNT growth reactions remains low, around 10% [3]. The poor efficiency has largely hindered the widespread use of CNTs in large-scale applications [4,5]. Hence there is a great need to find ways to improve catalytic efficiency and maintain high catalytic activity during CNT growth.

For CVD growth, the catalyst is typically composed of a transition metal deposited onto a substrate (for example SiO₂) as a thin film (5–10 Å) with or without a thin barrier layer [6]. During synthesis, the metal catalyst film, which is naturally oxidized after deposition, is heated up to high temperatures (typically between 400 and 800 °C) in a reducing environment (e.g. H₂). This causes dewetting and reduction of the catalyst film and results in the formation of reduced metallic nanoparticles. At this point, the catalyst is active and may seed the growth of CNTs while a gaseous carbon source is supplied. During the course of the reaction, the catalyst may undergo diffusion – on the substrate surface as well as into the substrate – which leads to particle coarsening and poisoning [7,8]. Other pathways for catalyst deactivation are metal evaporation, catalyst migration along the CNTs [9], alloying with inactive metals, and overcoating of the particles by graphitic carbon [10–12].

To efficiently produce CNTs it is necessary to both maximize the probability that a catalyst particle yields a CNT, the efficiency of carbon conversion from the gaseous carbon source, and the lifetime of CNT growth before the catalyst deactivates. Several strategies

---

have been applied to this end, a common one being the use of an Al_2O_3 layer, which stops diffusion, preventing coarsening and keeping the particle size small [13]. The Al_2O_3 layer also prevents alloying of the metal catalyst with the underlying SiO_2 substrate, which results in the formation of inactive metal silicides [14]. Other approaches involve catalyst pretreatment [15], using additives such as water [16], acetylene [17], and NH_3 [18], and tuning the catalyst support interaction through ion beam bombardment and oxidative pretreatment [19—22].

We have recently shown that the density of CNT forests can be dramatically increased by controlled exposure of the catalyst to trace hydrocarbon species during catalyst nanoparticle formation [23,24]. This "carbon preloading" significantly increases CNT forest density and ultimate height, compared to a well-controlled reference process without the trace carbon exposure. Furthermore, *in situ* ambient pressure X-ray photoelectron spectroscopy (AP-XPS) experiments also showed that hydrocarbon by-products from consecutive growths facilitated catalyst reduction and led to a significant increase in CNT number density. Interestingly, the use of carbon to reduce iron and other metals is widespread in industrial processes and dates back several millennia [25]. Carbothermal (or carbothermic) reactions, typically involving inexpensive coal as the carbon source and CO and CO_2 as the by-products, are used for reducing iron oxide to metallic iron. Even in the case of CNT growth, the carbon produced from the decomposition of acetylene has shown to be a better reducer of iron compared to hydrogen [26]. Our previous carbon preloading and AP-XPS results, as well as the catalyst deactivation pathway involving overcoating with graphitic carbon, pose questions regarding the nature and amount of carbon that is beneficial for CNT growth. For instance, what would happen if the carbon was in the form of a deposited amorphous film instead of in the form of trace hydrocarbons previously investigated? Is there a critical amount of carbon that maximizes CNT nucleation efficiency, growth rate, and/or yield?

To answer these questions, we systematically studied the effect of carbon preloading by performing single- and multi-walled carbon nanotube (SWCNT and MWCNT) growth experiments from a sputtered iron (Fe) catalyst coated with a sputtered carbon (C) film prior to dewetting. We studied the effect of the solid carbon preload with a combination of *in situ* techniques — Raman spectroscopy, AP-XPS ETEM. Our results show that an appropriate amount of carbon preload effectively produces more active Fe catalyst particles and reduces the incubation times of the activated particles, resulting in an increase CNT growth rates and yields.

2. Experimental

2.1. CNT growth on iron-carbon gradient

SWCNTs were grown in ARES™ (Autonomous Research System) [27—32], a cold-wall CVD reactor installed on a 2-axis motion stage above an inverted Raman microscope (Nikon Ti-E). The growth substrate consisted of 5 × 5 arrays of silicon micropillars (10 μm tall and 10 μm in diameter) spaced 50 μm apart on a thermally insulating SiO_2 sublayer. Each pillar was therefore thermally isolated and experiments were conducted by focusing a 532 nm laser (Spectra Physics Verdi V6) through a 50x objective lens; the laser served as the heat source as well as the Raman excitation source. The small thermal mass of the pillar combined with the high thermal resistance of the SiO_2 sublayer enabled heating to reaction temperatures within a fraction of a second when the laser power was varied in the 0—2.5 W range. The temperature-induced shift of the Si stokes and anti-stokes Raman bands (±520 cm^{-1}) was used to calculate the growth temperature. The accuracy of the temperature measurement is limited by the resolution of the ARES

spectrometer, and has been estimated to be approximately ±15 °C.

To see the effect of carbon preload thickness, we deposited thickness gradients of Fe catalyst and C, which were deposited sequentially and orthogonal to each other, where Fe deposition (0—1 nm) proceeded first (South Bay Technology Inc.), followed by rotation of the substrate by 90°and transfer to the C coater (Gatan) and C deposition (0—1.4 nm). The thickness profiles of the deposited Fe and C films were measured by Electron Probe Microanalysis (Cameca SX-100) and mapped with respect to the corresponding micropillars on the ARES substrate (Fig. S1 shows an image of the ARES substrate along with the Fe and C orthogonal gradients).

All experiments were conducted at a total pressure of 20 Torr, with a combination of ethylene (13.5 Torr) and hydrogen (6.5 Torr) gases as the hydrocarbon and catalyst reductant, respectively. The growth temperature was kept constant at ~(750 $\pm$ 15) °C; the error in the temperature stems from the uncertainty in calculating its value from the Raman frequency of the silicon substrate. Over 750 growth experiments were performed within the C and Fe thickness gradient. Raman spectra were collected continuously during each growth experiment. The integrated intensity of the Raman G band from the SWCNTs was calculated at the end of each experiment and plotted with respect to time to obtain a growth curve. Further Raman analysis was performed post-growth with a Renishaw inVia Raman microscope.

2.2. Environmental TEM experiments

In situ environmental TEM experiments were performed with an FEI Titan 80—300 ETEM at the Center for Functional Nanomaterials at Brookhaven National Laboratory. TEM grids with 10 nm thick Si_3N_4 windows (Norcada) were coated with 10 nm Al_2O_3 and 1 nm Fe in a similar fashion to that for AP-XPS experiments, as described above. One grid was additionally coated with a 1 nm carbon film as a preload. Before loading each sample, the ETEM was cleaned for 30 min with O2 plasma to remove carbon contaminants. CNT growth experiments were then performed by heating each sample in 40 mTorr H_2 to 650 °C and annealing for 15 min before introducing 10 mTorr C_2H_2 at that temperature to initiate CNT growth.

2.3. AP-XPS experiments

In addition to Raman analyses, we conducted AP-XPS experiments at the National Synchrotron Light Source II (NSLS II, 23-ID IOS beamline), at Brookhaven National Laboratory, to monitor the effect of carbon on catalyst populations during CNT growth. MWCNTs were grown using standard CVD recipes, with hydrogen as the reductant, ethylene as the carbon precursor gas, and catalyst-coated substrates mounted onto a heating element. A 1 nm Fe catalyst film was deposited, using magnetron sputtering, on a silicon catalyst support containing a 2—3 nm SiO_2 layer and a 10 nm Al_2O_3 layer (deposited using Atomic Layer Deposition). The Fe film was then kept either uncoated or coated with a 0.5 nm carbon film, also using magnetron sputtering. We note that in both the uncoated and C-coated samples, the Fe films were exposed to ambient conditions prior to carbon deposition and as such had become oxidized [24,33]. Each sample was 1) introduced to the AP-XPS chamber, 2) exposed to 50mTorr of hydrogen and heated to 750 °C (~20 °C/min), 3) exposed to ~500mTorr of ethylene at 750 °C, and 4) held under those conditions for ~13 min. XPS spectra were collected throughout these steps.
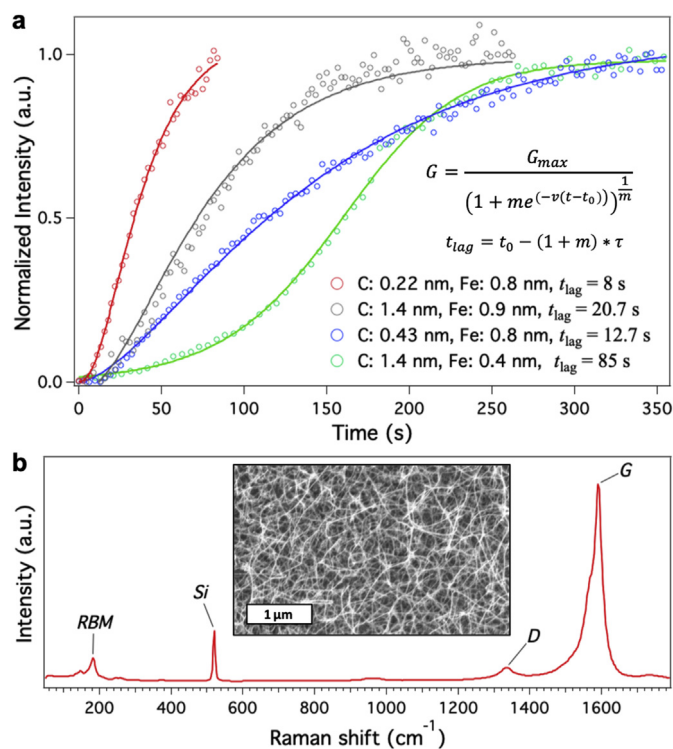
Fig. 1. (a) Representative normalized growth curves for various C and Fe thicknesses, fitted with the generalized logistic equation. The fitting equation and formula to calculate the lag times (t_{lag}) are in the inset. (b) Post-growth Raman spectrum from SWCNTs grown with 0.8/0.2 nm Fe/C, averaged from a two-dimensional map collected over the 10 μm micropillar array. Inset to (b) is a SEM image of the SWCNT bundles from this growth experiment. (A colour version of this figure can be viewed online.)

3. Results and discussion

3.1. In situ Raman studies

First, we discuss the influence of solid carbon preloading on the growth kinetics of SWCNTs using ARES. As described in greater detail in the Experimental Methods section, SWCNT growth experiments were performed by flowing ethylene and hydrogen (13.5 and 6.5 Torr partial pressures, respectively) through the chamber while individual pillars along the orthogonal gradient were heated to ~(750 ± 15) °C. Raman spectra were collected continuously (with 2s acquisition time) during each growth experiment. The integrated intensity of the SWCNT G band plotted against time yielded sigmoidal (S-shaped) growth curves, some examples of which are shown in Fig. 1a for various C and Fe film thicknesses. The growth curves were fitted by a generalized Logistic function (also known as the Richards curve [34]) as follows:

$$G = \frac{G_{max}}{(1 + me^{(-\nu(t-t_0))})^{\frac{1}{m}}} \quad (1)$$

Here G_{max} is the final G band intensity (proportional to the SWCNT yield), t_0 is the time at the inflection point of the sigmoidal curve, ν is the growth rate and m is a measure of the asymmetric nature of the sigmoidal growth curves. Therefore, G_{max}, t_0, ν and m were the four parameters used to fit the SWCNT growth curves. Also shown in Fig. 1a are the lag times for each of the growth curves, which are discussed in greater detail below. Fig. 1b shows a representative Raman spectrum, collected post-growth by mapping and averaging 121 spectra (11 × 11 array, with 1 μm spacing) over a micropillar. The averaged spectrum exhibits the typical

peaks found in the Raman spectra of SWCNTs — low frequency diameter-dependent radial breathing modes (RBMs), and the tangential C—C vibrational modes (G band). We note that Raman spectra measured before initiation of SWCNT growth did not exhibit any peaks from the solid C preload owing to the low thickness of the deposited carbon. The inset in Fig. 1b shows a scanning electron microscope (SEM) image collected from the corresponding micropillar. All of our growth experiments resulted in a mat of SWCNTs that grew by the root growth mechanism [27—29], and the RBM frequencies (150—300 cm^{-1}, Fig. 1a) indicate the diameter distribution of the SWCNTs to be between 0.9 and 2.0 nm.

We performed over 750 growth experiments in ARES over the entire range of Fe and C thicknesses, under the same CVD recipe. For each experiment, we calculated the SWCNT growth rates and yields from the *in situ* Raman data. Note that here we used the overall Raman intensity from the micropillar as a proxy for SWCNT yield and the maximum growth rates were obtained (in units of counts/s) from the linear portions of the sigmoidal growth curves (e.g., Fig. 1a). Thus, we can compare relative changes in both yield and growth rate as a function of C and Fe thickness. The results are shown as contour plots in Fig. 2, which were produced by performing Voronoi image interpolation (using Igor Pro) on the data. Looking at Fig. 2a, it is immediately apparent that the highest growth rate was achieved for a Fe/C thicknesses of 0.8/0.2 nm. Meanwhile, the SWCNT yields (Fig. 2b) exhibited a larger spread across the gradient but also peaked at approximately 0.8 nm Fe and 0.2 nm C. We also observed a corresponding increase in overall Raman intensity from these micropillars with a different laser excitation (633 nm; representative spectra collected post-growth and shown in Fig. S2), suggesting that the results presented in Fig. 2 are not limited by resonance effects.

The increases in SWCNT yields for a certain catalyst film thickness have been well documented in the literature. Studies of various supported catalyst films — Co [35,36], Ni [37], Fe [38] and CoMo [39,40] — have shown that, when growth is performed on a thickness gradient, a peak in the SWCNT yield is typically observed for catalyst thicknesses between 0.5 and 0.8 nm. Most of these previous studies focused on growth of vertically aligned SWCNTs (also called forests); forest heights are lower below the optimum thickness, and at greater catalyst film thicknesses the growth mode typically changes from single-to multi-walled carbon nanotubes (MWCNTs). Even though here we grew SWCNTs in the form of bundled mats rather than forests, we also observed an optimum catalyst thickness (~0.8 nm) for increased growth rates and yield of SWCNTs (Fig. S3).

What is very striking about Fig. 2, however, is that the SWCNT growth rates and yields were maximized with the exposure of the Fe catalyst to a small amount of solid C. This increase in growth rate and yield with solid C preloading is consistent with our previous reports for MWCNT forest growth [23], in which exposure of the catalyst film to trace hydrocarbons introduced in the gas phase was shown to accelerate catalyst nanoparticle formation by film dewetting, as well as influence iron oxide reduction to metallic iron [24]. These combined effects increased the probability of CNT nucleation, resulting in high density CNT forests. Here, by systematically studying well-defined thickness gradients of both C and Fe, we see that an increase in growth rate and yield is observed for a range of proportions of C and Fe (for example, ~0.2 nm C for an Fe thickness around 0.8 nm).

Having established that an appropriate amount of solid C preloading leads to an increase in SWCNT growth rate and yield, presumably by accelerating particle formation and reduction [23,24], we next investigate the effect of C on the growth kinetics by analyzing the growth curves. While all the ARES growth curves
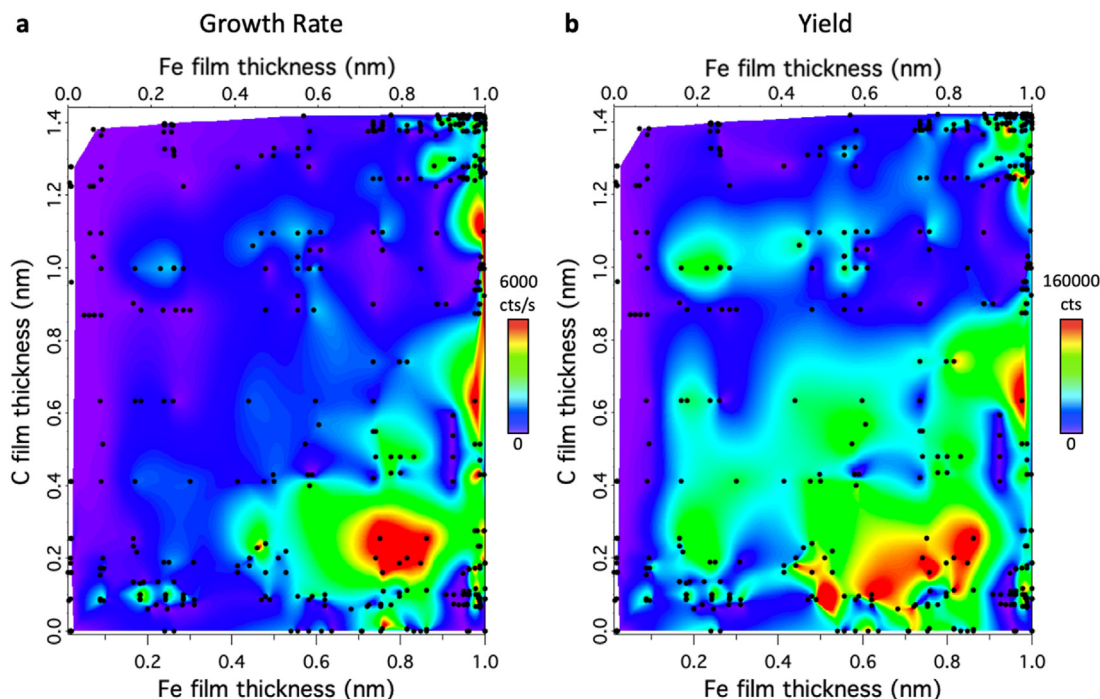
Fig. 2. Contour plots of (a) growth rate and (b) yield of SWCNTs as a function of C and Fe film thickness. The growth rates and yields were calculated by fitting the growth curves obtained from *in situ* Raman measurements with sigmoidal fits. Each data point in the figure corresponds to a growth experiment. (A colour version of this figure can be viewed online.)

were generally S-shaped (sigmoidal), their shape differed in terms of the anisotropy and location of the inflection point, *i.e.* the time when the growth rate is maximum. This can be seen in Fig. 1a, where the shapes of the growth curves range from highly asymmetric to fully symmetric. As mentioned above, we fitted the growth curves with a generalized Logistic function (Eq. (1)), which includes a parameter (m) that depends on the asymmetricity of the curve. When m equals −1, 0, and 1, the generalized Logistic equation reduces to the well-known self-exhausting, Gompertz and Logistic equations, respectively. All of these have been used to fit SWCNT growth curves in the literature [27,29,41,42].

One of the characteristics of a sigmoidal growth curve is the initial slow increase of growth before it becomes linear and achieves maximum growth rate. A characteristic time of the initiation of growth of CNT populations, which can be calculated from the sigmoidal fit, is the lag time (t_{lag}). In the case of SWCNT growth, it is the initial time period when a few tubes have nucleated and start growing, after which the growth density increases sufficiently to reach the maximum growth rate. Note that the lag time measured from the *in situ* Raman growth curves is different from what is typically called incubation time, which includes the period of carbon diffusion and segregation on to the surface of the catalyst particle, and subsequent formation of CNT nucleus (cap) [43–45]. The incubation time is followed by lift-off of the cap and elongation of the SWCNT [46,47], unless catalyst poisoning occurs. A short incubation time therefore corresponds to more nanotube nuclei and hence to an increase in nucleation probability and efficiency (*i.e.* a greater number of caps lift-off and grow nanotubes). While we could not measure the incubation time due to the relatively longer temporal resolution of our *in situ* Raman spectroscopy technique (2 s), we assume that the lag times estimated from the Raman spectra are proportional to the nucleation efficiencies of the catalyst particles and thus proportional to the SWCNT incubation times. The lag times were calculated from the generalized logistic

equation fit parameters according to the following equation:

$$t_{lag} = t_0 - (1 + m)*\tau \qquad (2)$$

Here t_0 is the time at the inflection point of the sigmoidal curve, τ is the time constant (lifetime) obtained from Equation (1), and m is a fitting parameter.

Fig. 3a plots the lag times as a function of C film thickness for a constant Fe thickness. Here we chose the Fe thickness to be 0.8 ± 0.1 nm. Remarkably, the lag times dip sharply (from ~15 s to 2.5 s) around 0.2 nm C; this C thickness also coincides with the maximum in the SWCNT yield (Fig. 2). A decrease in lag time concomitant with an increase in SWCNT growth rate and yield can also be observed for other Fe film thicknesses (Fig. S4 shows the lag time as a function of C film thickness for a Fe film thickness of ~1 nm). The correlation between reduced lag time and an increase in SWCNT growth rate and yield suggests that more Fe catalyst particles are available for growth. This would be possible if catalyst dewetting and formation as well as reduction was more efficient. Evidently an appropriate amount of carbon aids in both, and consequently results in better SWCNT growth.

To investigate the effect of solid C preloading on the SWCNT diameters, we performed *ex situ* Raman spectral mapping (using 514.5 nm excitation wavelength) and analysis. Low frequency RBM frequencies (ω_{RBM}) were extracted from 2D Raman maps (11 × 11 array with a 1 μm spacing between spots) collected over a number of micropillars, and the SWCNT diameters (d_t) were calculated according to the relation $d_t = 227/\omega_{RBM}$ [48]. Average SWCNT diameters (for a constant Fe thickness of 0.8 ± 0.1 nm) as a function of C film thickness are plotted in Fig. 3b, which shows a monotonic increase in average diameter with increasing C thickness. Note that this increase is small, although measurable, and goes from an average diameter of ~1.35 nm for the lowest carbon thickness to ~1.65 nm for 1 nm C. The C preload also affected the defect densities, which are commonly estimated from the ratio of intensities
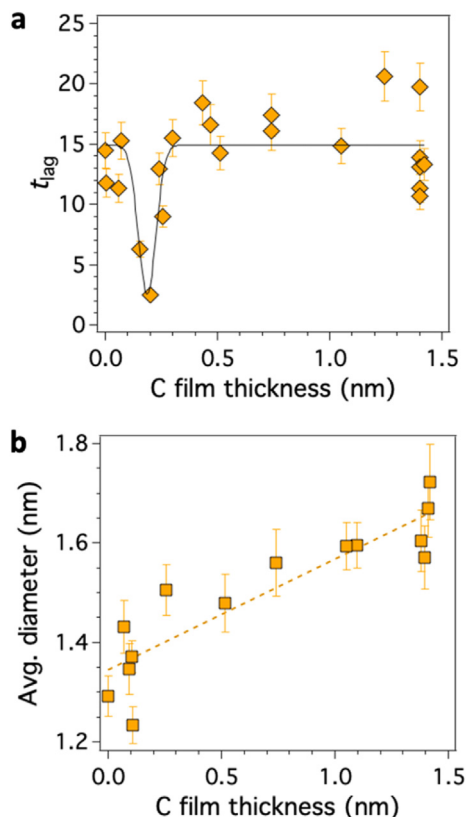
Fig. 3. (a) Lag times versus C film thickness for a constant Fe thickness (0.8 ± 0.1 nm). The lag time is lowest for a C thickness of approximately 0.2 nm, coinciding with a maximum in SWCNT growth rate and yield. The solid line is a guide to the eye. (b) Average SWCNT diameter versus C film thickness for a constant Fe thickness (0.8 ± 0.1 nm). (A colour version of this figure can be viewed online.)

of the disorder-induced D band to the graphitic G band. Higher I_D/I_G ratios were observed with increasing carbon (Fig. S5), indicating higher disorder with increasing C preloading, and consistent with the decrease in yield and growth rates with increasing C thickness.

3.2. In situ ETEM studies

To investigate the influence of solid C preload on catalyst particle formation, we turned to *in situ* ETEM experimentation. TEM grids with a 1 nm Fe catalyst film were used as the growth substrate inside an ETEM, with an additional 1 nm of C deposited in one case. Images were captured after annealing in 40 mTorr H_2 for 15 min at 650 °C and just prior to the introduction of the CNT growth precursor gas (C_2H_2), as seen in Fig. 4. After the 15 min H_2 annealing, the Fe film in the control sample appears to still be breaking apart (Fig. 4a), as indicated by the regions of lighter contrast (i.e. holes in the film). On the other hand, when C is present, the particles are visibly more well-formed (Fig. 4b) as evidenced by their more uniform round shape and spacing. Histograms of particle size distributions (Fig. 4c) obtained by image processing (applying a threshold and particle counting with ImageJ) show that there are many more particles available with C preload, indicating the solid C promotes more complete dewetting of the film. Thus, we can expect that the presence of C in contact with Fe during annealing in H_2 results in a lower incubation time, as was observed from the *in situ* Raman results. Moreover, it is noteworthy that the C preload results in an increase in the average particle diameter, corroborating the increase in average SWCNT diameter with C film thickness (Fig. 3b).
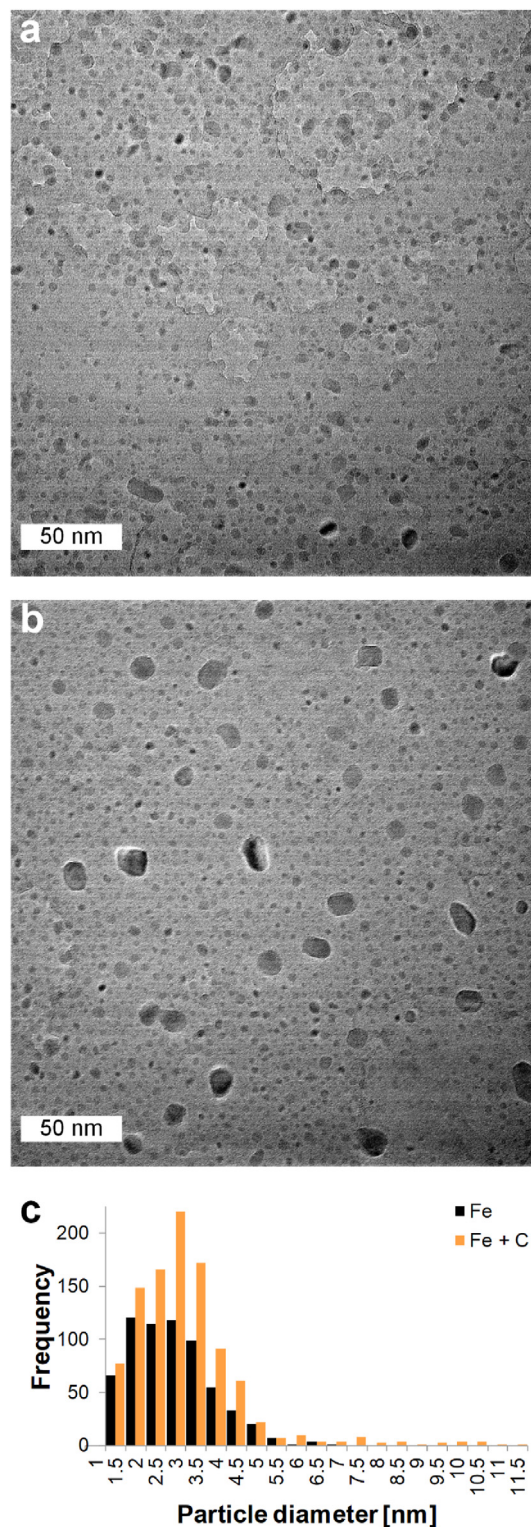

Fig. 4. ETEM images taken after annealing in 40 mTorr H_2 for 15 min, and just before introduction of C_2H_2 precursor for CNT growth, with (a) 1 nm Fe and (b) 1 nm Fe + 1 nm C. (c) The size distributions of particles found in the aforementioned images. (A colour version of this figure can be viewed online.)

3.3. In situ XPS studies

To gain further insight into the change in lag/incubation time caused by the solid C preload, we performed *in situ* XPS

experiments using conditions analogous to those used for the *in situ* Raman experiments. We examined two samples, one with a 1 nm iron film, and the other with 0.5 nm C sputtered on top of the 1 nm Fe film. The samples were exposed to reducing and growth conditions (see the Experimental section for details), and compared by monitoring the Fe 2p and C1s photoemission lines continuously. The waterfall plots in Figs. S6a and S6b show the evolution of the Fe 2p and C 1s emission lines, respectively, of both samples during reduction in hydrogen and growth in ethylene. From the waterfall plots, we obtained the temporal evolution of the various Fe and C valence states by first fitting the Fe 2p emission line with components corresponding to Fe^0, Fe^{2+} and Fe^{3+} [23], then by extracting the areas under the low spin components (Fe 2p3/2) corresponding to the aforementioned valence states, and by finally normalizing their sum to 100%. The resulting curves are plotted in Fig. 5a, along with the temperature versus time during the experiment (dashed line, right vertical axis). The reduction of the Fe film follows the pathway $Fe^{3+} \rightarrow Fe^{2+} \rightarrow Fe^0$, when exposed to hydrogen during annealing up to the growth temperature of 750 °C (before the introduction of ethylene). Therefore, over time the Fe^{3+} intensity is expected to decrease, followed by increases in intensity of the Fe^{2+} and Fe^0 states. These trends can be seen in Fig. 5a. Moreover, it is clear from Fig. 5a that the C/Fe sample reduces to both Fe^{2+} and Fe^0 at an earlier time and a lower temperature than the Fe film alone.

We also extracted the carbon accumulation rate from the area of the C 1s emission line once the ethylene was introduced (Fig. 5b) The accumulation rate exhibits a similar trend to that observed in the *in situ* Raman experiments; CNT growth starts much sooner from the C/Fe sample. One subtlety to note is that the *G* band intensity in the ARES experiments increases only after the CNTs start to grow, whereas the C1s intensity in the *in situ* XPS experiments increases as soon as carbon binds to the catalyst during stages

preceding growth (*i.e.* dewetting and incubation). Both curves in Fig. 5b were fit with Equation (1) and the calculated lag ties from Equation (2) are lower for the experiment performed with the solid C preload ($t_{lag} = 37$ s) compared to the control ($t_{lag} = 267$ s). We note that at the time of ethylene exposure, both samples exhibit similar degrees of reduction, and thus both of these particle populations are 'ready' to grow CNTs. Yet, the carbon preload samples exhibit CNT growth at an earlier point in time. This is presumably a consequence of having more incubated particles that have undergone the initial stages of growth, i.e. chemisorption and dissolution of carbon, and are able to nucleate as soon as the ethylene is introduced (Fig. S6b). Thus, we hypothesize that the solid C preload helps lower the nucleation barrier for CNTs, resulting in a greater fraction of nucleated particles. In contrast, the Fe particles without the C preload require a longer time before nucleation proceeds (Fig. S6a), suggesting that these have not undergone the early stages of growth but must do so in order to nucleate CNTs. The higher lag times in the AP-XPS measurements compared to those measured in from the *in situ* Raman measurements can be attributed to differences in the experimental techniques (rapid heating by a laser vs. slower resistive heating). Nevertheless, both sets of measurements show a clear reduction in lag times with the C preload. Regarding particle size distributions for the two samples, it is clear that the earlier reduction seen in Fig. 5a for the carbon preloaded sample will result in augmented particle coarsening, thus XPS results correlate well with the observed increase in average SWCNT diameter with increasing carbon thickness (Fig. 3b). Unmistakably, the carbon preloading allows the iron film to reduce earlier, coarsen more, and become incubated much earlier.

Taken together, our *in situ* Raman, ETEM and XPS results provide compelling evidence that solid C preload has the greatest impact on
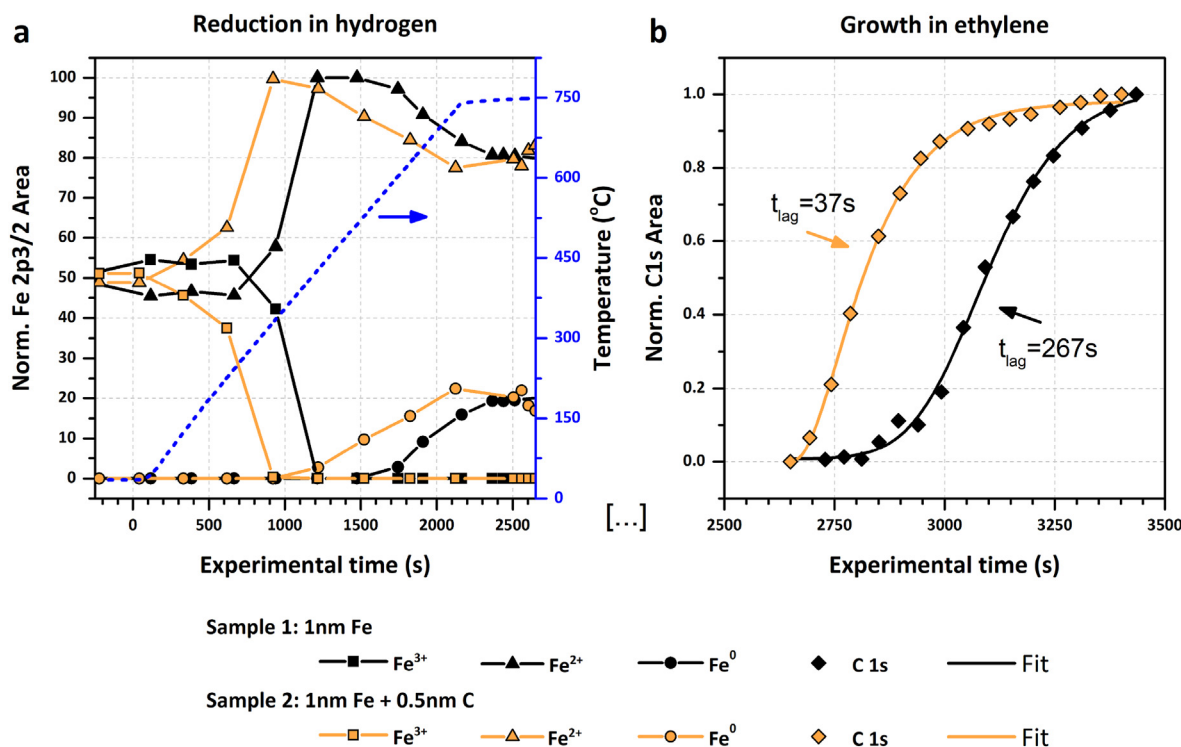

Fig. 5. (a) The evolution of the normalized Fe^{3+}, Fe^{2+} and Fe^0 valence states extracted from the Fe2p emission line shows the reduction of the iron films ($Fe^{3+} \rightarrow Fe^{2+} \rightarrow Fe^0$) in hydrogen when annealed prior to growth. The dashed line shows the increase in temperature (right vertical axis). (b) The carbon accumulation rate – obtained from the normalized C1s peak after introducing ethylene at 750 °C – shows the growth behavior for the two samples studied. Evidently, solid C preloading speeds up reduction and decreases the incubation time needed for CNT growth. (A colour version of this figure can be viewed online.)

the initial phase of synthesis, i.e. film reduction and dewetting, particle formation, and cap formation and lift-off (SWCNT nucleation). In other words, more particles are available and ready to grow CNTs with the aid of the solid C preload. The present results corroborate our previous findings with the exposure of the catalyst to trace hydrocarbons [23,24]. However, the thickness-dependent *in situ* Raman measurements showed how sensitive this is with respect to the amount of carbon. Indeed, previous reports on carbothermal treatment tin oxide [49], chromium oxide [50] and tungsten carbide [51] at the macro- and nano-scale have shown that the phase or size of the resulting product is sensitive to the amount of carbon used. Our observation of an optimum C film thickness (0.2 nm) shows a path forward for large-scale production of high yield CNTs by depositing a controlled amount of solid carbon on the Fe catalyst.

4. Conclusions

Here we have shown that we can increase the growth rate and yield of SWCNTs by depositing solid C on top of a thin Fe catalyst film. The increase is maximized for a specific carbon preload thickness, and in the case of our *in situ* Raman experiments, this thickness was ~0.2 nm. The C preload promotes the reduction of iron oxide and formation of Fe particles earlier, as observed in *situ* XPS measurements. Moreover, both Raman and XPS measurements revealed that the C preload helps to reduce incubation time, thus enabling CNT growth to begin sooner than the case of bare Fe catalyst particles. *In situ* ETEM measurements showed that the C preload also helped dewetting of the catalyst film, which resulted in a denser catalyst particle distribution. By employing multiple *in situ* techniques, we have shown that a little amount of deposited amorphous carbon can be very beneficial for CNT growth, allowing more catalyst particles to be ready and available for growth at the time of introduction of the hydrocarbon. Our results offer a simple and effective method to boost CNT yield and improve the efficiency of CVD growth of CNTs.

Declaration of competing interest

The authors declare that they have no known competing financial interests or personal relationships that could have appeared to influence the work reported in this paper.

CRediT authorship contribution statement

Rahul Rao: Investigation, Writing - original draft. **Jennifer Carpena-Núñez:** Investigation, Writing - review & editing. **Nicholas T. Dee:** Investigation, Writing - review & editing. **Dmitri N. Zakharov:** Investigation. **J. Anibal Boscoboinik:** Investigation. **Eric A. Stach:** Supervision, Writing - review & editing. **A. John Hart:** Supervision, Writing - review & editing. **Benji Maruyama:** Supervision, Writing - review & editing.

Acknowledgements

Appendix A. Supplementary data

Supplementary data to this article can be found online at https://doi.org/10.1016/j.carbon.2020.04.064.

References

[1] C.V. Thompson, Solid-state dewetting of thin films, Annu. Rev. Mater. Res. 42 (2012) 399—434.
[2] A.-C. Dupuis, The catalyst in the CCVD of carbon nanotubes - a review, Prog. Mater. Sci. 50 (2005) 929—961.
[3] M. Ishida, H. Hongo, F. Nihey, Y. Ochiai, Diameter-controlled carbon nanotubes grown from lithographically defined nanoparticles, Jpn. J. Appl. Phys. 43 (10B) (2004) L1356.
[4] R. Rao, C.L. Pint, A.E. Islam, R.S. Weatherup, S. Hofmann, E.R. Meshot, et al., Carbon nanotubes and related nanomaterials: critical advances and challenges for synthesis toward mainstream commercial applications, ACS Nano 12 (12) (2018) 11756—11784.
[5] M.F.L. De Volder, S.H. Tawfick, R.H. Baughman, A.J. Hart, Carbon nanotubes: present and future commercial applications, Science 339 (6119) (2013) 535—539.
[6] A. Moisala, A. Nasibulin, E. Kauppinen, The role of metal nanoparticles in the catalytic production of single-walled carbon nanotubes—a review, J. Phys. Condens. Matter 15 (2003) S3011.
[7] P.B. Amama, C.L. Pint, L. McJilton, S.M. Kim, E.A. Stach, P.T. Murray, et al., Role of water in super growth of single-walled carbon nanotube carpets, Nano Lett. 9 (2009) 44—49.
[8] S.M. Kim, C.L. Pint, P.B. Amama, D.N. Zakharov, R.H. Hauge, B. Maruyama, et al., Evolution in catalyst morphology leads to carbon nanotube growth termination, J. Phys. Chem. Lett. 1 (6) (2010) 918—922.
[9] S. Jeong, J. Lee, H.-C. Kim, J.Y. Hwang, B.-C. Ku, D.N. Zakharov, et al., Direct observation of morphological evolution of a catalyst during carbon nanotube forest growth: new insights into growth and growth termination, Nanoscale 8 (4) (2016) 2055—2062.
[10] A.I. La Cava, C.A. Bernardo, D.L. Trimm, Studies of deactivation of metals by carbon deposition, Carbon 20 (3) (1982) 219—223.
[11] A.A. Puretzky, D.B. Geohegan, S. Jesse, Ivanov IN, and Eres G, in situ measurements and modeling of carbon nanotube array growth kinetics during chemical vapor deposition, Appl. Phys. A 81 (2) (2005) 223—240.
[12] M. Stadermann, S.P. Sherlock, J.-B. In, F. Fornasiero, H.G. Park, A.B. Artyukhin, et al., Mechanism and kinetics of growth termination in controlled chemical vapor deposition growth of multiwall carbon nanotube Arrays, Nano Lett. 9 (2) (2009) 738—744.
[13] P.B. Amama, C.L. Pint, S.M. Kim, L. McJilton, K.G. Eyink, E.A. Stach, et al., Influence of alumina type on the evolution and activity of alumina-supported Fe catalysts in single-walled carbon nanotube carpet growth, ACS Nano 4 (2) (2010) 895—904.
[14] Y. Homma, Y. Kobayashi, T. Ogino, D. Takagi, R. Ito, Y.J. Jung, et al., Role of transition metal catalysts in single-walled carbon nanotube growth in chemical vapor deposition, J. Phys. Chem. B 107 (44) (2003) 12161—12164.
[15] C. Zhang, R. Xie, B. Chen, J. Yang, G. Zhong, J. Robertson, High density carbon nanotube growth using a plasma pretreated catalyst, Carbon 53 (2013) 339—345.
[16] D.N. Futaba, K. Hata, T. Namai, T. Yamada, K. Mizuno, Y. Hayamizu, et al., 84% catalyst activity of water-assisted growth of single walled carbon nanotube forest characterization by a statistical and macroscopic approach, J. Phys. Chem. B 110 (15) (2006) 8035—8038.
[17] R. Xiang, E. Einarsson, J. Okawa, Y. Miyauchi, S. Maruyama, Acetylene-accelerated alcohol catalytic chemical vapor deposition growth of vertically aligned single-walled carbon nanotubes, J. Phys. Chem. C 113 (18) (2009) 7511—7515.
[18] Z.Y. Juang, I.P. Chien, J.F. Lai, T.S. Lai, C.H. Tsai, The effects of ammonia on the growth of large-scale patterned aligned carbon nanotubes using thermal chemical vapor deposition method, Diam. Relat. Mater. 13 (4) (2004) 1203—1209.
[19] A.E. Islam, P. Nikolaev, P.B. Amama, S. Saber, D. Zakharov, D. Huffman, et al., Engineering the activity and lifetime of heterogeneous catalysts for carbon nanotube growth via substrate ion beam bombardment, Nano Lett. 14 (9) (2014) 4997—5003.
[20] N. Yang, M. Li, J. Patscheider, S.K. Youn, H.G. Park, A forest of sub-1.5-nm-wide single-walled carbon nanotubes over an engineered alumina support, Sci. Rep. 7 (2017) 46725.
[21] S. Esconjauregui, M. Fouquet, B.C. Bayer, S. Eslava, S. Khachadorian, S. Hofmann, et al., Manipulation of the Catalyst-Support Interactions for Inducing Nanotube Forest Growth, vol. 109, 2011 (4): 044303.
[22] P.B. Amama, C.L. Pint, F. Mirri, M. Pasquali, R.H. Hauge, B. Maruyama,

Catalyst—support interactions and their influence in water-assisted carbon nanotube carpet growth, Carbon 50 (7) (2012) 2396—2406.

[23] N.T. Dee, J. Li, A. Orbaek White, C. Jacob, W. Shi, P.R. Kidambi, et al., Carbon-assisted catalyst pretreatment enables straightforward synthesis of high-density carbon nanotube forests, Carbon 153 (2019) 196—205.

[24] J. Carpena-Núñez, J.A. Boscoboinik, S. Saber, R. Rao, J.-Q. Zhong, M.R. Maschmann, et al., Isolating the roles of hydrogen exposure and trace carbon contamination on the formation of active catalyst populations for carbon nanotube growth, ACS Nano 13 (2019) 8736—8748.

[25] B.V. L'vov, Mechanism of carbothermal reduction of iron, cobalt, nickel and copper oxides, Thermochim. Acta 360 (2) (2000) 109—120.

[26] M. Bedewy, B. Viswanath, E.R. Meshot, D.N. Zakharov, E.A. Stach, A.J. Hart, Measurement of the dewetting, nucleation, and deactivation kinetics of carbon nanotube population growth by environmental transmission electron microscopy, Chem. Mater. 28 (11) (2016) 3804—3813.

[27] R. Rao, D. Liptak, T. Cherukuri, B.I. Yakobson, B. Maruyama, In situ evidence for chirality-dependent growth rates of individual carbon nanotubes, Nat. Mater. 11 (2) (2012) 1—4.

[28] R. Rao, N. Pierce, D. Liptak, D. Hooper, G. Sargent, S.L. Semiatin, et al., Revealing the impact of catalyst phase transition on carbon nanotube growth by in SituRaman spectroscopy, ACS Nano 7 (2) (2013) 1100—1107.

[29] P. Nikolaev, D. Hooper, N. Perea-López, M. Terrones, B. Maruyama, Discovery of wall-selective carbon nanotube growth conditions via automated experimentation, ACS Nano 8 (10) (2014) 10214—10222.

[30] R. Rao, A.E. Islam, N. Pierce, P. Nikolaev, B. Maruyama, Chiral angle-dependent defect evolution in CVD-grown single-walled carbon nanotubes, Carbon 95 (2015) 287—291.

[31] P.N. Nikolaev, D. Hooper, F. Webber, R. Rao, K. Decker, M. Krein, et al., Autonomy in materials research: a case study in carbon nanotube growth, npj Computational Materials 2 (2016) 16031.

[32] E.J. Kluender, J.L. Hedrick, K.A. Brown, R. Rao, B. Meckes, J.S. Du, et al., Catalyst discovery through megalibraries of nanomaterials, Proc. Natl. Acad. Sci. Unit. States Am. 116 (1) (2019) 40—45.

[33] P.B. Amama, D. Zemlyanov, B. Sundarakannan, R.S. Katiyar, T.S. Fisher, XPS and Raman characterization of single-walled carbon nanotubes grown from pre-treated Fe2O3 nanoparticles, Jpn. J. Appl. Phys. 41 (16) (2008) 165306.

[34] F.J. Richards, A flexible growth function for empirical use, J. Exp. Bot. 10 (2) (1959) 290—301.

[35] S. Noda, H. Sugime, K. Hasegawa, K. Kakehi, Y. Shiratori, A simple combinatorial method aiding research on single-walled carbon nanotube growth on substrates, Jpn. J. Appl. Phys. 49 (2) (2010), 02BA02.

[36] K. Kakehi, S. Noda, S. Maruyama, Y. Yamaguchi, Growth valley dividing single- and multi-walled carbon nanotubes: combinatorial study of nominal thickness of Co catalyst, Jpn. J. Appl. Phys. 47 (4R) (2008) 1961.

[37] K. Kakehi, S. Noda, S. Chiashi, S. Maruyama, Supported Ni catalysts from

[38] K. Hasegawa, S. Noda, Real-time monitoring of millimeter-tall vertically aligned single-walled carbon nanotube growth on combinatorial catalyst library, Jpn. J. Appl. Phys. 49 (2010), 0855104.

[39] H. Navas, B. Maruyama, K. Weaver, M. Paillet, A.-A. Zahab, F. Fossard, et al., Interplay of interfacial compounds, catalyst thickness and carbon precursor supply in the selectivity of single-walled carbon nanotube growth, Carbon 80 (2014) 599—609.

[40] H. Sugime, S. Noda, S. Maruyama, Y. Yamaguchi, Multiple "optimum" conditions for Co—Mo catalyzed growth of vertically aligned single-walled carbon nanotube forests, Carbon 47 (1) (2009) 234—241.

[41] D. Futaba, K. Hata, T. Yamada, K. Mizuno, M. Yumura, S. Iijima, Kinetics of water-assisted single-walled carbon nanotube synthesis revealed by a time-evolution analysis, Phys. Rev. Lett. 95 (5) (2005) 56104.

[42] P. Finnie, A. Li-Pook-Than, J. Lefebvre, The dynamics of the nucleation, growth and termination of single-walled carbon nanotubes from in situ Raman spectroscopy during chemical vapor deposition, Nano Res 2 (2009) 783.

[43] M. Moors, H. Amara, T. Visart de BocarmeÃÂ, C. Bichara, F. Ducastelle, N. Kruse, et al., Early stages in the nucleation process of carbon nanotubes, ACS Nano 3 (3) (2009) 511—516.

[44] I. Wako, T. Chokan, D. Takagi, S. Chiashi, Y. Homma, Direct observation of single-walled carbon nanotube growth processes in situ scanning electron microscopy, Chem. Phys. Lett. 449 (4—6) (2007) 309—313.

[45] A. Li-Pook-Than, J. Lefebvre, P. Finnie, Phases of carbon nanotube growth and population evolution from in situ Raman spectroscopy during chemical vapor deposition, J. Phys. Chem. C 114 (25) (2010) 11018—11025.

[46] E. Pigos, E.S. Penev, M.A. Ribas, R. Sharma, B.I. Yakobson, A.R. Harutyunyan, Carbon nanotube nucleation driven by catalyst morphology dynamics, ACS Nano 5 (12) (2011) 10096—10101.

[47] R. Rao, R. Sharma, F. Abild-Pedersen, J.K. Norskov, A.R. Harutyunyan, Insights into carbon nanotube nucleation: cap formation governed by catalyst interfacial step flow, Sci. Rep. 4 (2014) 6510.

[48] P.T. Araujo, I.O. Maciel, P.B.C. Pesce, M.A. Pimenta, S.K. Doorn, H. Qian, et al., Nature of the constant factor in the relation between radial breathing mode frequency and tube diameter for single-wall carbon nanotubes, Phys. Rev. B 77 (24) (2008) 241403.

[49] R. Padilla, H.Y. Sohn, The reduction of stannic oxide with carbon, Metallurgical Transactions B 10 (1) (1979) 109—115.

[50] L.M. Berger, S. Stolle, W. Gruner, K. Wetzig, Investigation of the carbothermal reduction process of chromium oxide by micro- and lab-scale methods, Int. J. Refract. Metals Hard Mater. 19 (2) (2001) 109—121.

[51] R. Polini, E. Palmieri, G. Marcheselli, Nanostructured tungsten carbide synthesis by carbothermic reduction of scheelite: a comprehensive study, Int. J. Refract. Metals Hard Mater. 51 (2015) 289—300.

nominal monolayer grow single-walled carbon nanotubes, Chem. Phys. Lett. 428 (4) (2006) 381—385.